Monolayer Hexagonal Boron Nitride: An Efficient Electron Blocking Layer in Organic Photovoltaics

Citation: Tavakoli, M. M., Park, J.-H., Mwaura, J., Saravanapavanantham, M., Bulović, V., Kong, J., Monolayer Hexagonal Boron Nitride: An Efficient Electron Blocking Layer in Organic Photovoltaics. Adv. Funct. Mater. 2021, 31, 2101238

As Published: http://dx.doi.org/10.1002/adfm.202101238

Publisher: Wiley

Persistent URL: https://hdl.handle.net/1721.1/140279

Version: Author's final manuscript: final author's manuscript post peer review, without publisher's formatting or copy editing

Monolayer Hexagonal Boron Nitride (h-BN), an Efficient Electron Blocking Layer in Organic Photovoltaics

Mohammad Mahdi Tavakoli,* Ji-Hoon Park, Jeremiah Mwaura, Mayuran Saravanapavanantham, Vladimir Bulović, Jing Kong*

Department of Electrical Engineering and Computer Science, Massachusetts Institute of Technology, Cambridge, 02139 MA, USA

* Corresponding author: mtavakol@mit.edu; jingkong@mit.edu

Abstract

Finding a suitable stable and solution-processable electron blocking layer (EBL) for organic photovoltaics (OPVs) is one of the main challenges for the fabrication of efficient, stable, large-area and flexible OPVs. In this study, we propose a monolayer hexagonal boron nitride (h-BN) grown by chemical vapor deposition (CVD) as an effective EBL for the OPVs. Unexpectedly, we found that h-BN can replace the commonly used hole transport layers (HTLs), *i.e.*, molybdenum trioxide (MoO_3) and poly(3,4-ethylenedioxythiophene) polystyrene sulfonate (PEDOT:PSS) in an inverted device architecture. We here employed a wet-transfer technique and successfully placed a single layer of h-BN on top of the PV2000:$PC_{60}BM$ blend. Analysis of the bandgap diagram showed that the monolayer h-BN makes smaller barrier for holes but significantly larger barrier for electrons. This makes the h-BN effective in blocking electrons while creating a possible path for the holes through

tunneling to the electrode, due to the low energy barrier at the PV2000/h-BN interface. Using h-BN as an EBL, we achieve efficient inverted OPVs with an average solar-to-power conversion efficiency (PCE) of 6.13%, which is comparable with reference devices based on MoO_3 (7.3%) and PEDOT:PSS (7.6%) as HTLs. Interestingly, our devices with h-BN shows great light-soak stability when compared to the MoO_3-based OPVs. Our study reveals that the monolayer h-BN grown by CVD could be an effective alternative EBL for the fabrication of efficient, lightweight and stable OPVs.

Keywords: Electron blocking layer, h-BN, Organic, Solar cell, Efficiency, Stability

Introduction

Organic photovoltaics (OPVs) are one of the most attractive types of thin film solar cells owning to their solution processing, ease of fabrication, low-cost, bandgap tunability, great flexibility and low-temperature processing.[1-6] Researchers in the field of OPVs have synthesized various types of organic molecules including donors and non-fullerene acceptors (NFA) in order to improve the light absorption and thus efficiency as well as air stability.[7-11] These great efforts have led to a relative PCE enhancement of ~40% for OPVs over the last two years.[12] For instance, Yuan et al.[13] reported a new class of NFA, Y6, which increased the PCE of OPVs up to 15.7%. Later, other researchers by either developing this molecule or using a ternary blend achieved a PCE of over 17%.[14,15] This impressive progress has kept the

OPVs among the fastest growing solar cell technologies similar to perovskite solar cells (PSCs).[16,17]

Apart from efficiency, stability is one of the key factors for the commercialization purposes.[18] Regarding the stability of OPVs, there have been some progress made in terms of the molecular structure of both donor and acceptor or interface engineering, however, there is still a long path here to fully address this issue.[19-24] Particularly for high-efficiency devices, use of new NFAs with an infrared absorption and having more complicated chemical structures but with typically a lower air-stability is required.[25,26] Developing more stable molecular structure with better optical absorption and charge mobility is a major key to overcoming this shortcoming.[27] Besides the active layer, charge transport and interfacial layers could be another reason for the instability exhibited by OPVs.[28] In this regard, hole transport layers (HTLs) are more vulnerable to degradation under light illumination and bending tests.[29,30] For the larger scale fabrication of OPV modules, it is desired that all layers be deposited through solution processing techniques (roll-to-roll for example), with one of the most commonly used HTL being poly(3,4-ethylenedioxythiophene):poly(styrenesulfonate) (PEDOT:PSS).[31,32] It is a fact that finding alternative HTLs with better stability can significantly improve the overall lifetime stability of the OPVs.

Two-dimensional (2D) materials, especially graphene, have attracted many researchers in the field of solar cells due to their exciting optoelectronic properties.[33-35] Since the scaling trend in the photovoltaic (PV) technology is moving toward lighter and thinner devices, the

atomically thin structure and great flexibility of 2D materials make them ideal candidates for the next generation of thin film PVs.[36,37] For instance, monolayer graphene has shown great potential to be used as top and bottom electrodes in the thin film solar cells.[38-41] In addition to graphene, transition-metal dichalcogenides (TMDs) such as MoS_2 have been also reported as interfacial or transport layer in the PVs.[42] However, these materials are still far away from real applications due to scale-up manufacturing challenges and there still remains room for further development in this direction.

Hexagonal boron nitride (h-BN) is another type of 2D materials, which has not been employed or reported yet in any solar cell device application, since it is an isolating material and has a huge bandgap.[43] Normally, h-BN is used as a gate dielectric, supporting substrate or an encapsulation layer in field effect transistors or quantum transport devices.[44] In this study, we for the first time demonstrate the application of h-BN in organic solar cells. We employed the monolayer h-BN as an EBL in both conventional and inverted structures of OPVs and achieved working devices with PCEs of 4.8% and 6.13%, respectively, comparable with the reference cells' performance. The band diagram indicates that the monolayer h-BN effectively hinders the electron transfer while allowing the holes to reach the electrode through a tunneling mechanism due to smaller energy barrier. Moreover, the h-BN-based devices shows excellent operational stability.

Results and Discussions

In this work, we grew the h-BN on copper foil using a CVD method as explained in the experimental section. A wet-transfer technique was then employed to apply the h-BN on top

of the indium-doped tin oxide (ITO) and on top of the active layer blend **Figures 1a** and **1b** illustrate the optical images of the h-BN transferred on SiO_2/Si substrate and a zoomed image of h-BN after removing the PMMA, respectively. By carefully removing the residual PMAA, we obtained a clean h-BN monolayer on substrates for the deposition step (Figure 1b). **Figure 1c** shows the Raman spectrum of the h-BN transferred on the SiO_2/Si substrate. The strong peak located at 1370 cm^{-1} is the characteristic peak of the h-BN, indicating its presence on the SiO_2/Si substrate. Another peak at 1450 cm^{-1} corresponds to the silicon.[45] **Figure 1d** demonstrates the UV-visible spectrum of the h-BN on glass, which indicates a bandgap of 5.8 eV for the h-BN.

To evaluate the role of h-BN in the device, we fabricated OPVs with both inverted and conventional architectures. Here, we used PV2000:PC_{60}BM blend as an active layer for our devices since it shows a great air-stability.[46] We considered ITO/ZnO/Blend/b-BN/Ag and ITO/h-BN/Blend/ZnO nanocrystals/Ag structures for inverted and conventional designs, respectively. As explained in the experimental section, the h-BN was transferred on ITO and on the active layer blend using PMMA as a supporting polymer. Afterward, the PMMA was removed by acetone in order to achieve monolayer h-BN (F**igures S1** and **S2**). **Figure 2a** depicts the schematic of an inverted OPV with a monolayer of h-BN as an EBL, verified by a cross-sectional scanning electron microscopy (SEM) image shown in **Figure 2b**. In order to have a fair comparison, we fabricated OPVs without and with h-BN, MoO_3 and PEDOT:PSS as HTLs. The photovoltaic (PV) results of these devices are shown in **Figure 2c**. **Table 1**

shows a summary of the current density (J)- voltage (V) results for the corresponding devices.

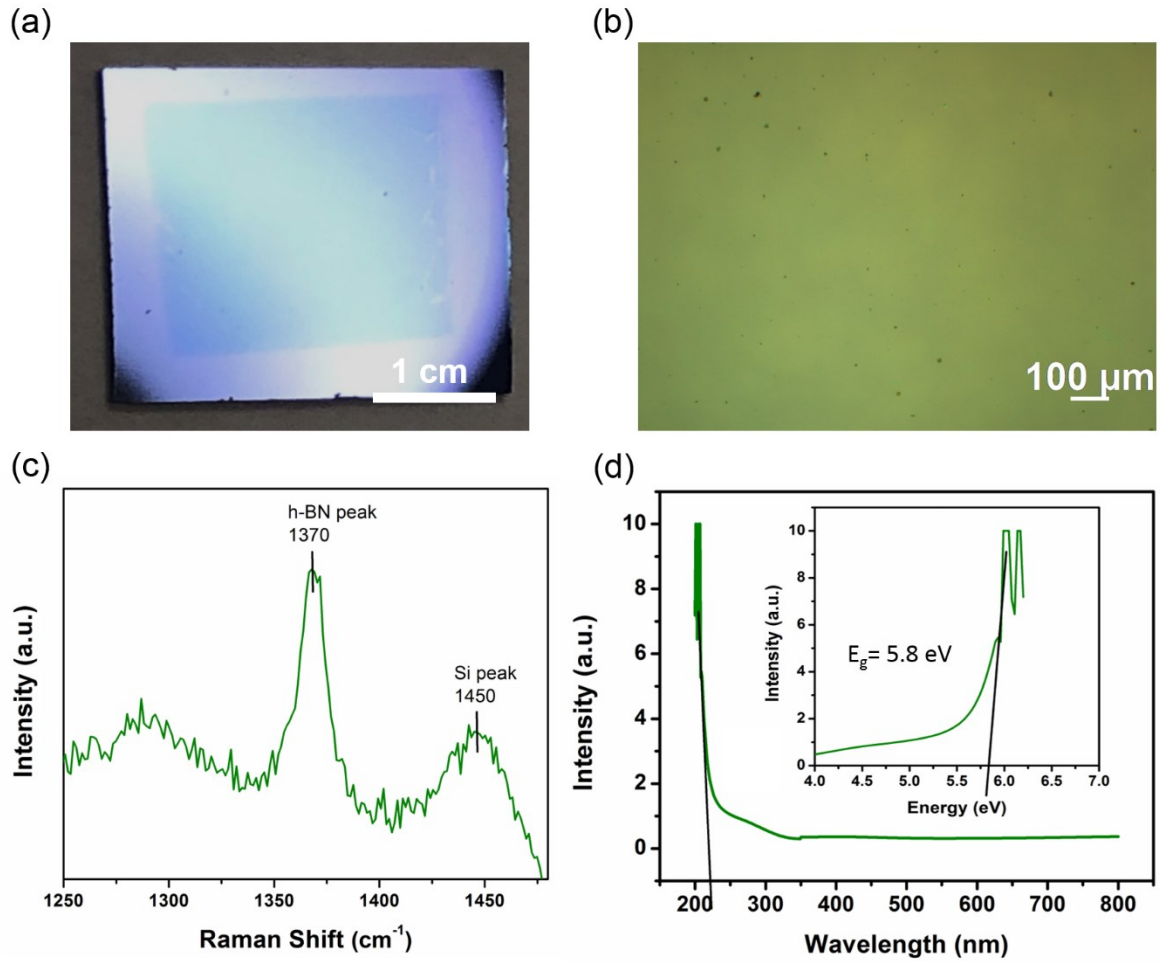

Figure 1. (a) Photograph of the h-BN monolayer transferred on silicon oxide. (b) Optical image of the h-BN monolayer taken using optical microscope, indicating a clean surface after removing PMMA. (c) Raman spectrum and (d) UV-visible spectra of the h-BN. The inset image in **Figure 1d** shows the bandgap measurement of the h-BN monolayer.

As seen, the device without HTL shows a very low open circuit voltage (V_{OC}) of 0.323 V due to the carrier recombination at the PV2000/Ag interface, which results in a poor PCE of 2.1%. This indicates the significant role of the HTL in OPVs. Here, OPVs with both inorganic (MoO_3) and organic HTLs (PEDOT:PSS) were fabricated and their PV results were compared with OPVs with h-BN. The device with MoO_3 shows a V_{OC} of 0.775 V, a short circuit current density (J_{SC}) of 13.68 mA/cm^2, a fill factor (FF) of 69% and a PCE of 7.3%. By using PEDOT:PSS, the PCE is improved slightly to 7.6%, due to having better V_{OC} and FF. Interestingly, the device with h-BN shows impressive PV results with a PCE of 6.13% (V_{OC}: 0.754 V: 12.92 mA/cm^2, FF: 63%), which are comparable with the reference OPVs. The average PV results of the 10 devices for each configuration are shown in **Figure S3**, which is in good agreement with the results of best performing devices (**Table 1**). In fact, the average values of PV parameters of h-BN based OPVs are only slightly lower than those of reference devices, thus showing the potential of h-BN as an alternative EBLs in the OPVs. To further investigate the value of J_{SC} in our devices, we performed external quantum efficiency (EQE) for all devices, as shown **in Figure 2d**. As results indicates, the devices with HTL shows higher EQE and thus J_{SC}, than the devices without HTL. The EQE value is highest for device with the PEDOT:PSS as HTL. The extracted J_{SC} values from EQE spectra are listed in Table 1, which well-matches with the J-V curves shown in **Figure 2c.**

To further study the device architecture, we also fabricated solar cells with conventional structure, as schematically shown in **Figure 3a**. The cross-sectional SEM image of the OPV with ITO/h-BN/PV2000:$PC_{60}BM$/ZnO NCs/Ag is illustrated in **Figure 3b**. In this structure,

the fabrication process is started with the h-BN transfer. **Figure 3c** shows the J-V curves of the OPVs without HTL and with h-BN and PEDOT:PSS. **Table 2** lists the PV parameters of the corresponding devices. The role of HTL is more obvious in this architecture, where the device without a HTL shows a very low PCE of 0.8%, similar to a shorted device. The device with PEDOT:PSS HTL shows a high PCE of 6.85%, highlighting the role of an effective HTL.

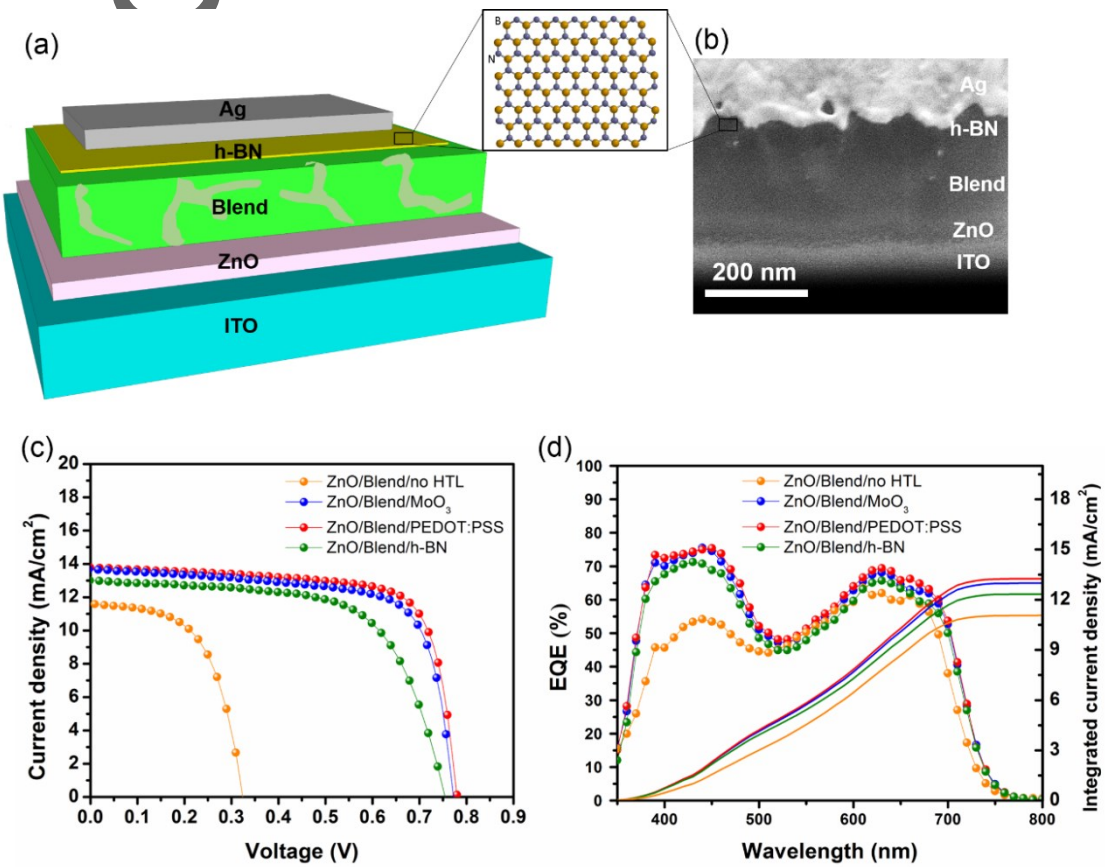

Figure 2. (a) Schematic and (b) cross-sectional SEM image of the OPV with inverted architecture. (c) J-V curves and (d) EQE spectra of the OPVs without HTL and with MoO_3, PEDOT:PSS and h-BN.

Table 1. PV parameters of the inverted OPVs without HTL and with MoO_3, PEDOT:PSS or h-BN. (The average PCE values are shown in parentheses)

Device configuration	V_{oc} (V)	J_{sc} (mA/cm^2)	FF (%)	PCE (%)	J_{sc} form EQE (mA/cm^2)
ITO/ZnO/Blend/Ag (no HTL)	0.323	11.59	55	2.1 (1.93)	11.2
ITO/ZnO/Blend/MoO_3/Ag	0.775	13.68	69	7.3 (7.21)	13.05
ITO/ZnO/Blend/PEDOT:PSS/Ag	0.78	13.77	71	7.6 (7.5)	13.21
ITO/ZnO/Blend/h-BN/Ag	0.754	12.92	63	6.13 (6.07)	12.34

Intriguingly, the devices with h-BN in a conventional design also works with a decent PCE of 4.8%. This efficiency is less than the inverted h-BN-based OPV, possibly due the band alignment or the defects incurred during the transfer. **Figure 3d** shows the EQE spectra of the OPVs without and with PEDOT:PSS and h-BN. The extracted J_{SC} values obtained by integration of the EQE over the solar spectrum are shown in **Table 2**, and are in good agreement with the J-V results. The average PV results of the representative OPVs are summarized in **Figure S4**, showing the same trend as the best performing devices.

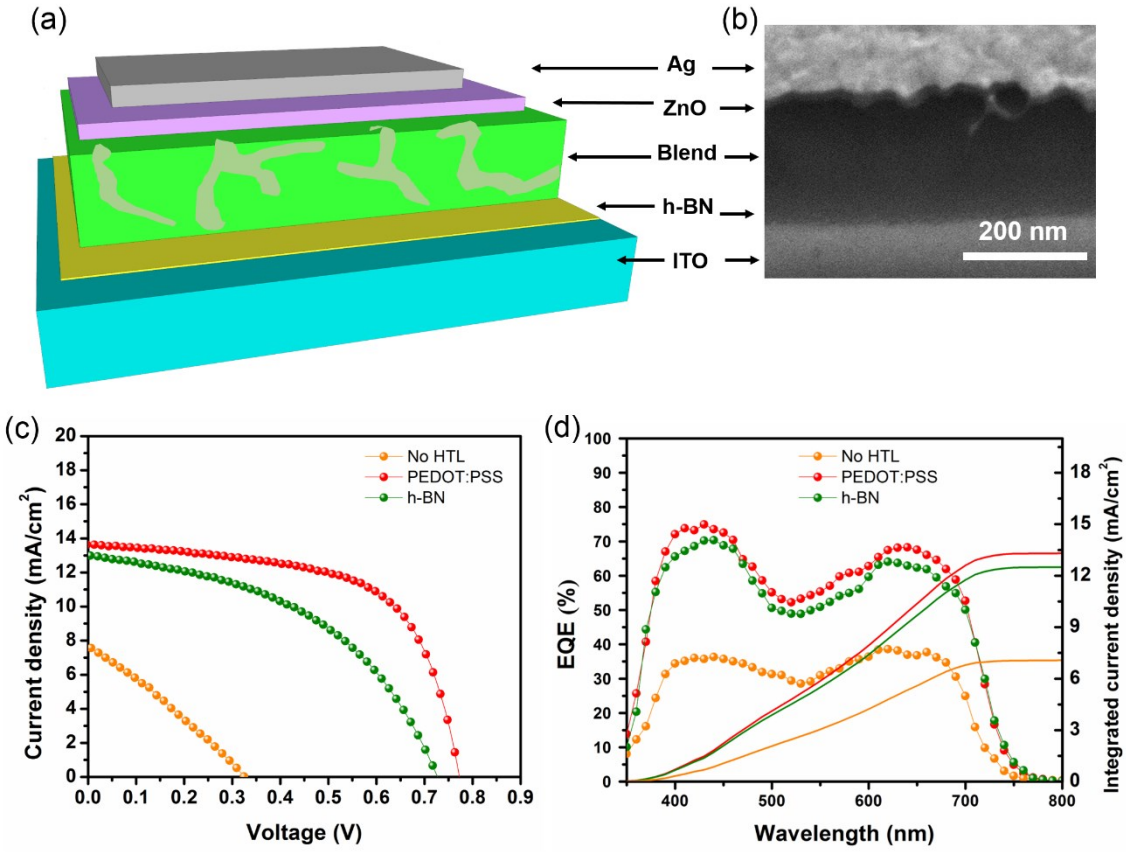

Figure 3. (a) Schematic and (b) cross-sectional SEM image of the OPV with conventional architecture. (c) J-V curves and (d) EQE spectra of the OPVs without HTL and with PEDOT:PSS and h-BN.

Table 2. PV parameters of the conventional OPVs without HTL and with PEDOT:PSS and h-BN. (The average PCE values are shown inside parentheses)

Device configuration	V_{oc} (V)	J_{sc} (mA/cm^2)	FF (%)	PCE (%)	J_{sc} form EQE (mA/cm^2)
ITO/Blend/ZnO/Ag (no HTL)	0.348	7.57	30	0.8 (0.69)	7.1
ITO/PEDOT:PSS/Blend/ZnO/Ag	0.773	13.65	65	6.85 (6.2)	13.3
ITO/h-BN/Blend/ZnO/Ag	0.727	12.95	51	4.8 (4.2)	12.48

To further investigate the role of h-BN in the OPVs, the photoluminescence (PL) spectra of the PV2000 films without and with different HTLs on ITO glasses were measured (**Figure 4a**). The samples with different HTLs shows strong quenching effect compared with the pure PV2000 film, indicating a fast charge transfer from the PV2000 to the ITO glass through the HTLs. Among these HTLs, PEDOT:PSS shows the strongest quenching effect, which is in good agreement with its performance in devices. For the case of h-BN, we fabricated the h-BN/PV2000 film sample on glass and measured its PL again. Interestingly, this time we did not observe any quenching effect in this sample **(Figure S5).** This result indicates that the holes could not transfer to the h-BN alone due to the presence of a small barrier between PV2000 and h-BN layers. However, with the sample on ITO glass, the transfer most likely occurs through tunneling. **Figure S6** shows the time-resolved PL (TRPL) measurement of the ITO/h-BN/PV2000, ITO/PEDOT:PSS/PV2000 and ITO/MoO_3/PV2000 samples. We have fitted the curves using a biexponential equation and extracted the lifetime of these samples. We found that the ITO/PEDOT:PSS/PV2000 has the shortest lifetime due to the stronger quenching effect of the PEDOT:PSS HTL. Interestingly, the ITO/h-BN/PV2000 sample

shows strong quenching effect but slightly weaker than its counterparts. Consequently, the dynamic charge transfer could take place in the h-BN based device comparable with other types of HTL.

We also studied the band alignment of these samples using ultraviolet photoelectron spectroscopy (UPS). **Figures 4b** and **S7** demonstrate the UPS results of the h-BN and PV2000 samples, respectively. Based on these results and the values from literature,[47,48] band diagrams of the OPVs with both inverted and conventional architectures were plotted in **Figures 4c** and **4d**, respectively. The UPS results indicate that the h-BN has a valence band (VB) of -5.86 eV and a conduction band (CB) of -0.06 eV. In contrast, the PV2000 shows the highest occupied molecule orbital (HOMO) of -5.65 eV and the lowest un-occupied molecular orbital (LUMO) of -3.98 eV and hence, h-BN can effectively block the electron transfer at PV2000/h-BN interface due to its huge barrier for the electrons (3.92 eV). However, for the case of hole transfer, the barrier is smaller (0.21 eV) and thus, there is a higher possibility for hole tunneling through monolayer h-BN, as also confirmed by PL results (**Figure S5)**.

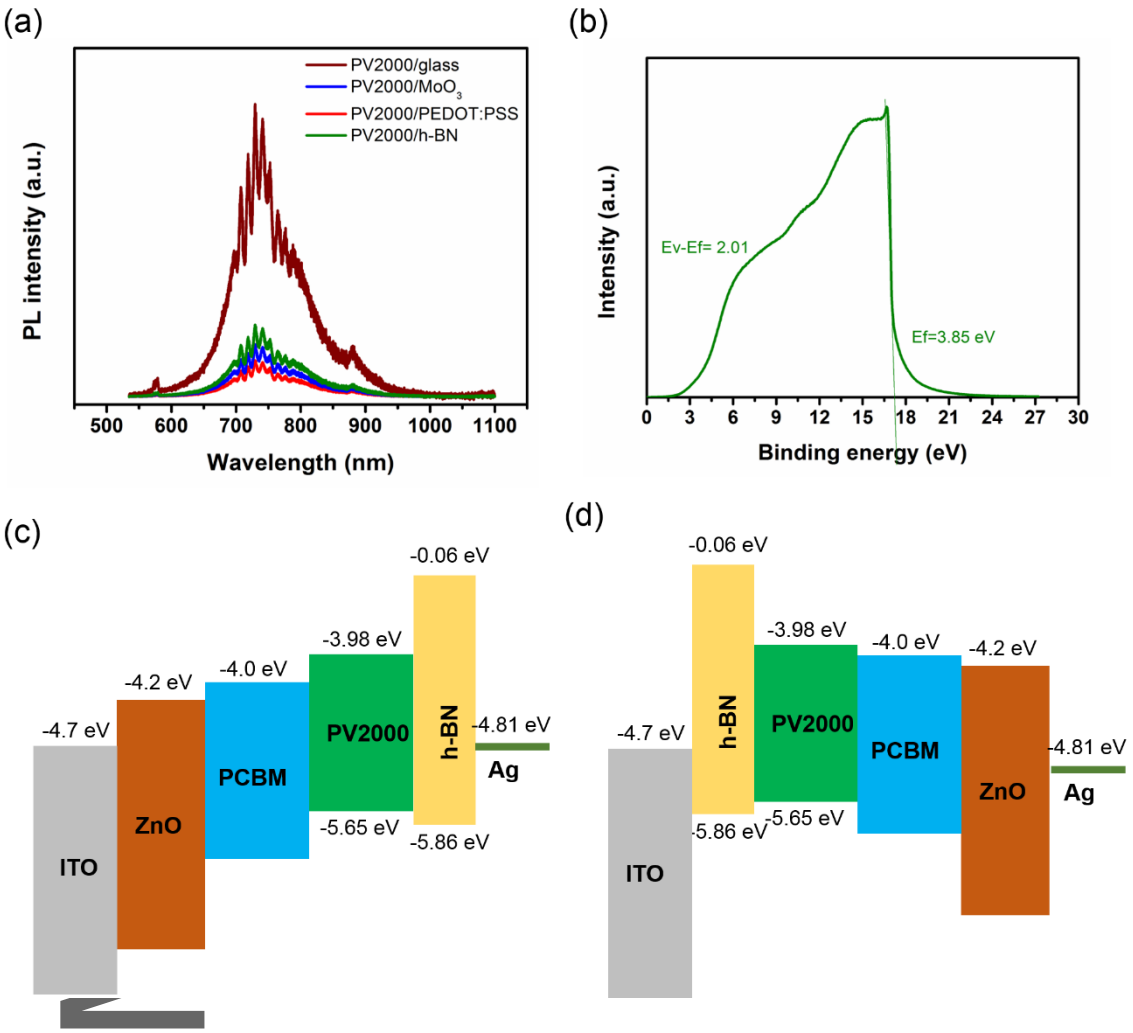

Figure 4. (a) Photoluminescence spectra of the PV2000, PV2000/MoO_3, PV2000/PEDOT:PSS and PV2000/h-BN films on ITO glasses. (b) UPS measurement of the h-BN monolayer. Band diagrams of the h-BN-based OPVs with inverted (c) and conventional (d) architectures.

, Because the ITO and silver electrodes have comparable work functions, the h-BN performs similarly in both the inverted and conventional device architectures.

Beside above results, we also studied the role of the back metal contact in the PV results by considering three different metal electrodes, Al, Ag and Au with the inverted structure. **Figure 5a** shows the J-V curves of the devices with different electrodes with PV performances results of the corresponding devices summarized in **Table 3**. From the results, the devices with h-BN/Au back contact shows the highest PCE of 6.53%. h-BN/Ag based device demonstrates slightly lower PCE than the h-BN/Au device, but much better that the h-BN/Al one. From the average PV results shown in **Figure S8**, the difference in PV results for the case of h-BN/Ag and h-BN/Au is originated mostly from FF and $V_{OC.}$ With the h-BN/Al however, all PV parameters are lower than h-BN/Ag. The EQE spectra and the extracted J_{SC} values (**Figure 5b**) confirmed that the J_{SC} in both h-BN/Ag and h-BN/Au are identical but in the case of h-BN/Al is the lowest value. These results highlight the role of electrode work function on the efficiency of h-BN-based OPVs. To further analyze these results, the band diagrams of these OPVs were plotted by measuring the work functions of different electrodes using UPS. **Figure 5c** shows the UPS results of different metals, indicating work functions of -4.34 eV, -4.81 eV and -5.15 eV for Al, Ag and Au electrodes, respectively. **Figure 5d** illustrates the band diagrams of the corresponding devices. Since Au has the deepest work function, the barrier for the hole transfer would be lower that its counterpart devices. Therefore, the tunneling effect is more efficient in h-BN/Au based OPVs, resulting in improved PV results.

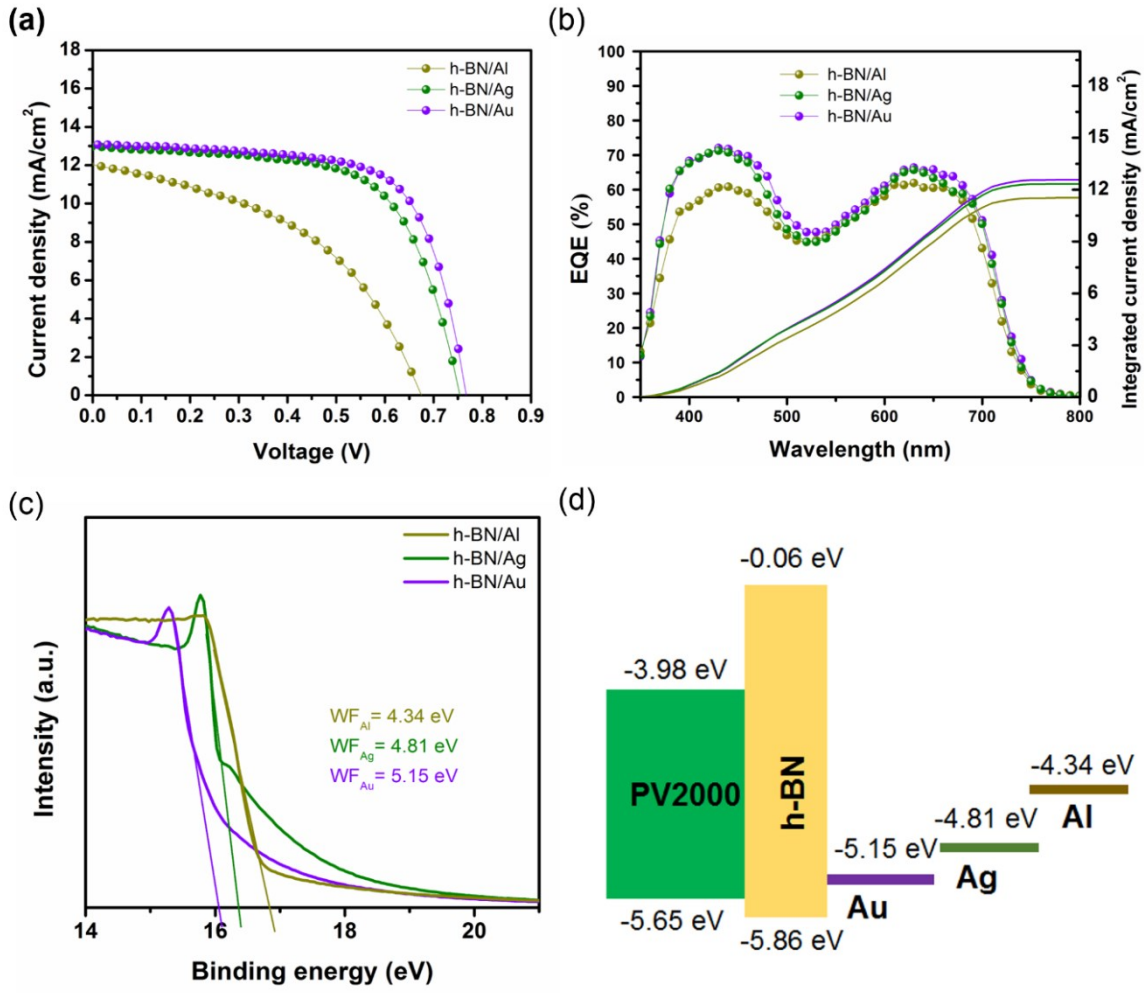

Figure 5. (a) J-V curves and (b) EQE spectra of the OPVs with h-BN/Al, h-BN/Ag and h-BN/Au back contacts. (c) UPS measurement and (d) band diagram of the OPVs with h-BN/Al, h-BN/Ag and h-BN/Au back contacts.

Table 3. PV parameters of the inverted OPVs with h-BN/Al, h-BN/Ag and h-BN/Au back contacts. (The average PCEs are shown in parentheses)

Device configuration	V_{oc} (V)	J_{sc} (mA/cm^2)	FF (%)	PCE (%)	J_{sc} form EQE (mA/cm^2)
ITO/ZnO/Blend/h-BN/Al	0.675	11.85	52	4.16 (3.96)	11.53
ITO/ZnO/Blend/h-BN/Ag	0.754	12.92	63	6.13 (6.07)	12.34
ITO/ZnO/Blend/h-BN/Au	0.768	13.1	65	6.53 (6.27)	12.55

In order to analyze our devices based on various transporting layers, we evaluated them using the transient photovoltage (TPV), transient photocurrent (TPC), dark I-V and electrochemical impedance spectroscopy (EIS) measurements. Charge carrier lifetime and charge extraction ability were studied by the TPV (**Figure S9a**) and TPC (**Figure S9b**) measurements, respectively. The results indicate that the PEDOT:PSS based device has the longest charge recombination decay time together with the shortest charge extraction time. The MoO_3 based device also shows similar TPV and TPC results to the PEDO:PSS one. Interestingly, the h-BN based device shows slightly lower charge recombination decay time and a bit higher charge extraction time compared with its counterparts. These results can explain the slightly lower V_{OC} and J_{SC} in the h-BN based device. **Figure S9c** shows the dark current measurement of the corresponding devices. As seen, the h-BN based device depicts slightly larger dark current as compared to other devices, indicating more recombination and thus lower V_{OC} in this device.

We also analyzed our devices using EIS measurement. **Figure S9d** demonstrates the Nyquist plots of the corresponding devices in this study. The inset image in **Figure S9d** shows the equivalent circuit for fitting purpose (R_S: series resistance; R_{rec}: recombination resistance). After estimation of the R_S by fitting, the device with PEDOT:PSS shows the lowest R_S and h-BN based device indicates the highest R_S. The lower FF in the h-BN based device can be correlated to the higher series resistance in this device. Additionally, the h-BN based OPV shows the slightly lower R_{rec} compared with other devices, indicating more carrier recombination in this device. As a results, slightly lower V_{OC} in the h-BN based OPV most likely can be explained by its higher carrier recombination. Notably, the results of these characterizations for all transporting layers in OPVs are so close and the slightly lower PV parameters in the h-BN based devices can be explained by the above characterizations. This indicates that the h-BN could be a good alternative for either MoO_3 or PEDOT:PSS HTLs, since the charge transfer occurs properly in this device, possibly using the tunneling effect. In this study, we also evaluated the lifetime stability of unencapsulated OPVs with different HTLs (without any encapsulation) using ISOS protocols[49] as stability is a one of the key factors for commercialization purposes. **Figure 6a** shows the shelf-life stability results of the corresponding devices measured in ambient (40% relative humidity (RH)) under dark condition. Since both MoO_3 and PEDOT:PSS are sensitive to moisture, the PCE of these devices are dropped to 93% and 82% of their initial PCE values, respectively, after 35 days. In contrast, the h-BN based devices exhibited better shelf-life stability with less than 2% PCE loss. **Figure 6b** shows the operational stability result of these devices under continuous

illumination and nitrogen flow. In this test, we also observed the same trend in stability results, where the devices with h-BN shows only 13% PCE loss, which is much better than those with MoO_3 (22%) and PEDOT:PSS (40%) HTLs. Additionally, we evaluated the thermal stability of these devices under dark condition and at 85 °C, as shown in Figure 6c. As seen, the h-BN device shows a great thermal stability with almost no change in PCE after maintaining the device at 85 °C for 10 days. However, the devices with MoO_3 and especially PEDOT:PSS HTLs degrade faster in the same condition. These results show that h-BN has a stable molecular structure in both ambient and under illumination and it can function as a protection layer for various materials. Beside working as an electron blocking layer, the h-BN protects the device from possible ion migration from the electrode side to the active layer and thus preventing shunting during stability tests. These PCE and stability results suggest that the h-BN can be a good alternative to replace other HTLs in the OPV devices.

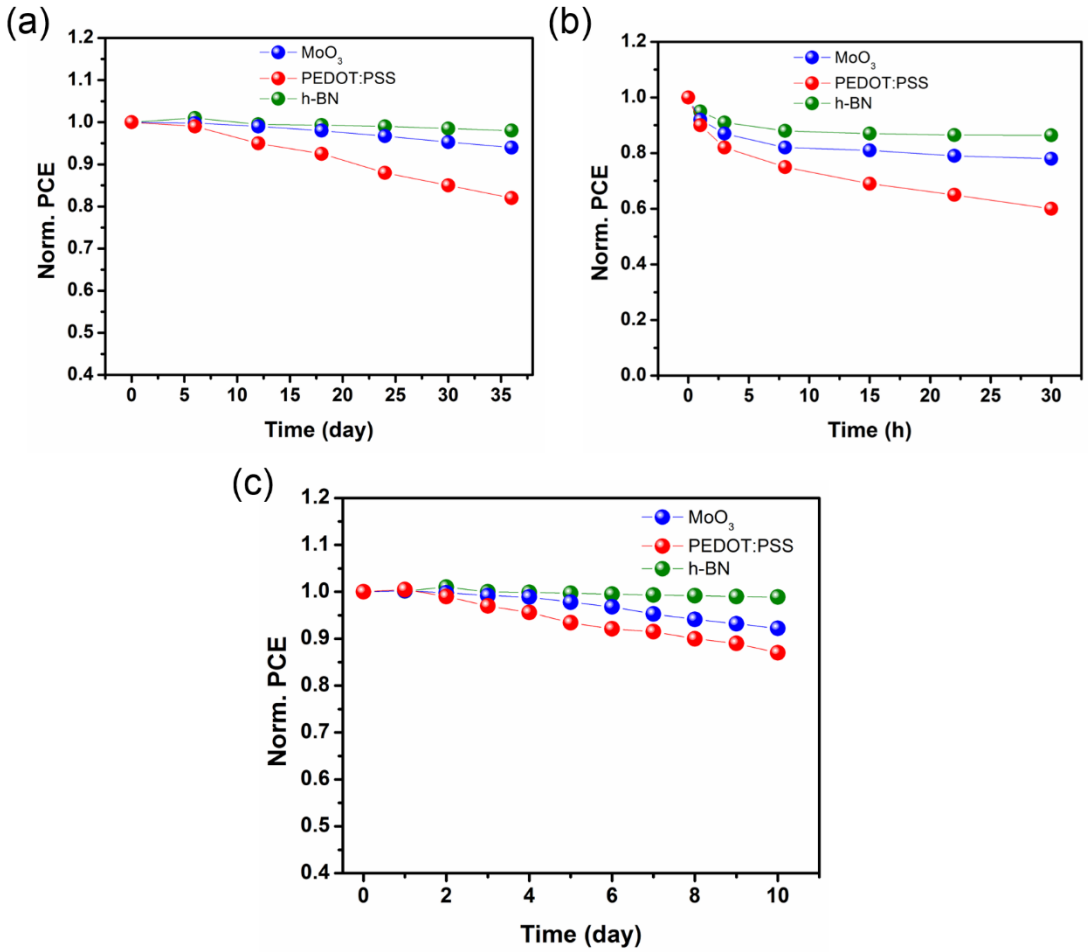

Figure 6. Shelf-life (a) operational (b) and thermal (c) stability measurements of the OPVs with MoO_3, PEDOT:PSS and h-BN. All stability measurement were performed according to the ISOS protocols.

Conclusion:

In summary, we synthesized a high-quality h-BN monolayer using CVD process and demonstrated its effectiveness an alternative EBL for OPVs. We employed a wet-transfer technique for device fabrication and successfully fabricated OPVs with both inverted and

conventional designs. We find that the devices work well with h-BN in both cases. Using h-BN as an EBL, OPVs with PCEs of 6.13% and 4.8% for inverted and conventional device structures were achieved respectively, which were comparable with the OPVs based on commonly-used HTLs. The band alignment results proved that the h-BN can effectively block electrons and there is only a small barrier for the hole transfer to the electrodes. The PL results confirmed of the possibility of tunneling for the holes in h-BN-based OPVs due to the small energy barrier between the HOMO level of PV2000 and the work function of the electrode. Using gold contact electrode with deeper work function further reduces this barrier, leading to an improved PCE. More interestingly, the h-BN-based OPVs show better shelf-life and operational stability compared to devices with either MoO_3 or PEDOT:PSS HTLs. These results highlight the advantages of using the h-BN monolayer as a 2D interface material in OPVs.

Experimental Section:

Synthesis of h-BN

For continuous monolayer h-BN film growth, a CVD technique was employed and a Cu foil (100 um thickness, Nilaco Corporation) was placed at the center of a quartz tube with a diameter of one inch. Then, the temperature was increased to 1070 °C for 30 min under a flow of 10 sccm of H_2 gas and maintained in this condition for 10 min in order to the temperature stabilization. Monolayer h-BN was grown from the reaction of borazine (0.6 sccm) with hydrogen (10 sccm) in 30 minutes. Finally, the furnace was turned down to room temperature quickly to achieve high quality h-BN.

h-BN transfer:

After growth of h-BN on copper foil, a wet-transfer technique was employed to place the h-BN on either ITO or PV2000:$PC_{60}BM$ blend film. For this purpose, PMMA was used as a supporting polymer and the copper was etched away using a copper etchant solution. After etching, a stack of h-BN/PMMA was transferred in a water bath. Finally, the stack was scooped by the target substrates, followed by removing the PMMA using acetone, which resulted in transferring monolayer h-BN on either ITO or blend film.

Device fabrication:

First, the ITO substrates were cleaned using ultrasonic for 20 min in different baths, triton X100 (1 vol% diluted in deionized (DI) water), DI water, acetone, ethanol. These substrates were further cleaned by oxygen plasma for 5 min before any deposition. For the inverted design, a ZnO solution was prepared by dissolving zinc acetate dihydrate (0.3 M, Sigma-Aldrich) and ethanolamine (0.18 mL, Sigma-Aldrich) in 2-methoxyethanol (Sigma-Aldrich) and deposited on ITO glasses using spin-coating at 4000 rpm for 45 s, followed by 10 min annealing at 220 °C. For the conventional design, PEDOT:PSS solution was spin-coated at 2500 rpm for 40 s, followed by 10 min annealing at 140 °C. For the h-BN-based device, the h-BN was transferred onto the ITO using a wet-transfer technique. Afterward, the blend solution (42 mg/mL) was prepared by dissolving PV2000 (Raynergy Tek) and $PC_{60}BM$ with a ratio of 1:2 in o-xylene solvent by stirring at 75 °C overnight. This solution was spin-coated at 1000 rpm for 40 s, followed by annealing at 120 °C for 3 min. The whole fabrication process was performed in ambient condition (40% RH). In the inverted design, the h-BN was

transferred on the blend active layer using a wet-transfer approach, PEDOT:PSS was deposited using spin-coating at 2500 rpm for 40 s, followed by 2 min annealing at 100 °C, MoO_3 was thermally evaporated on the blend (12 nm) at a rate of 0.5 Å/s. In the conventional design, the ZnO NCs as an ETL was spin-coated at 3000 rpm for 30 s, followed by 2 min annealing at 100 °C. Finally, the devices were completed by deposition of 100 nm-thick metal electrodes (Al, Ag, Au) using thermal evaporation at a rate of 0.5 Å/s.

Film characterization:

To study the cross-sectional images, a focused ion beam (FIB) scanning electron microscopy (SEM, Helios) was employed. Varian Cary 5. Was used to measure the UV-visible spectra. PL and Raman spectra were recorded a HORIBA Jobin-Yvon HR800 system using a WITec alpha 300 confocal Raman microscope. TRPL curves was measured using a picosecond pulsed diode laser with excitation wavelength of λ=405 nm and pulse width of 49 ps. The curves were fitted by biexponential equation of $I(t) = a_i \exp(-t/\tau_i)$ (a_i and τ_i are the amplitude and the lifetime respectively). UPS measurement was performed using AXIS NOVA (Kratos Analytical Ltd, UK), which was equipped by a He I (21.2 eV) photon source.

Device measurement:

J-V measurement was performed using a standard xenon lamp (450-watt, Oriel, USA) and a Keithley (model 2400, USA). In this measurement, the solar simulator was adjusted to 1000 W/m^2 according to the AM1.5 G condition using a standard silicon solar cell (Newport). A shadow mask was used to obtain a device area of 0.054 cm^2. During the measurement, the voltage scan rate and the dwell time were 10 mVs^{-1} and 15 s, respectively. The external

quantum efficiency (EQE) was measured by a QEPVSI-B, Newport to evaluate the J_{SC} results. Stability tests were performed according to ISOS protocols.[49] For the shelf-life stability test, the devices were kept in ambient (40% RH) under dark conditions and measured over time. For the operational stability, the devices were maintained under continuous illumination inside a N_2-filled glovebox and their PCE was monitored over time. Thermal stability was performed under dark and at 85 °C. Electrochemical impedance spectroscopy (EIS) measurement was performed using a Solartron analyzer under 0 bias and dark condition. The frequency was 0.1 Hz to 1 MHz. TPV and TPC decay measurements were recorded by a digital oscilloscope (Tektronix TDS 3052C).

Acknowledgement

This work was sponsored by Eni S.p.A under the Massachusetts Intestine of Technology Energy Initiative (MITEI) Solar Frontier Center.

References

1. R. Po, C. Carbonera, A. Bernardi, N. Camaioni, *Energy Environ. Sci.* 2011, **4,** 285-310.

2. Y. Song, S. Chang, S. Gradecak, J. Kong, *Adv. Energy Mater.* 2011, **6**, 1600847.

3. C. Y. Chang, L. Zuo, H. L. Yip, Y. Li, C. Z. Li, C. S. Hsu, Y. J. Cheng, H.. Chen, A. K. Y. Jen, *Adv. Funct. Mater*. 2013, **23**, 5084–5090.

4. S. Li, L. Ye, W. Zhao, H. Yan, B. Yang, D. Liu, W. Li, H. Ade and J. Hou, *J. Am. Chem. Soc.*, 2018, **140**, 7159–7167

5. C.-Y. Liao, Y. Chen, C.-C. Lee, G. Wang, N.-W. Teng, C.-H. Lee, W.-L. Li, Y.-K. Chen, C.-H. Li, H.-L. Ho, P. H.-S. Tan, B. Wang, Y.-C. Huang, R. M. Young, M. R. Wasielewski, T. J. Marks, Y.-M. Chang and A. Facchetti, *Joule*, 2019, **4**, 189–206.

6. J. Liu, L.-K. Ma, H. Lin, L. Zhang, Z. Li, W. K. Law, A. Shang, H. Hu, W. Ma, H. Yan, *Small Methods* 2018, **2**, 1700415.

7. M. M. Tavakoli, J. Zhao, R. Po, G. Bianchi, A. Cominetti, C. Carbonera and J. Kong, *Adv. Funct. Mater.*, 2019, **29**, 1905887.

8. J. Hou, Q. Inganäs, R.H. Friend, F. Gao, *Nat. Mater.* 2018, **17***,* 119.

9. R. Po, J. Roncali, *J. Mater. Chem. C* 2016, **4**, 3677-3685.

10. D. Hu, Q. Yang, H. Chen, F. Wobben, V. M. Le Corre, R. Singh, T. Liu, R. Ma, H. Tang, L. J. A. Koster, T. Duan, H. Yan, Z. Kan, Z. Xiao and S. Lu, *Energy Environ. Sci.*, 2020, **13**, 2134–2141.

11. Y. Li, L. Zhong, B. Gautam, H.-J. Bin, J.-D. Lin, F.-P. Wu, Z. Zhang, Z.-Q. Jiang, Z.-G. Zhang, K. Gundogdu, Y. Li and L.-S. Liao, *Energy Environ. Sci.*, 2017, **10**, 1610–1620.

12. National Center for Photovoltaics (NCPV) at the National Renewable Energy Laboratory (NREL), www.nrel.gov/pv/assets/images/efficiency-chart.png (accessed: March 2020).

13. J. Yuan, Y. Zhang, L. Zhou, G. Zhang, H. L. Yip, T. K. Lau, X. Lu, C. Zhu, H. Peng, P. A. Johnson, M. Leclerc, *Joule*, 2019, **3**, 1140-1151.

14. Y. Lin, Y. Firdaus, M. I. Nugraha, F. Liu, S. Karuthedath, A. H. Emwas, W. Zhang, A. Seitkhan, M. Neophytou, H. Faber, E. Yengel, *Adv. Sci.* 2020, **7**, 1903419.

15. L. Zhan, S. Li, T.K. Lau, Y. Cui, X. Lu, M. Shi, C. Z. Li, H. Li, J. Hou, H. Chen, *Energy Environ. Sci.* 2020*,* **13**, 635-645.

16. M. H. Gharahcheshmeh, M. M. Tavakoli, E. F. Gleason, M. T. Robinson, J. Kong, K. K. Gleason, *Sci. Adv.* 2019, **5**, eaay0414.

17. M. M. Tavakoli, P. Yadav, R. Tavakoli, J. Kong, *Adv. Energy Mater.* 2018, **8**, 1800794.

18. M. M. Tavakoli, R. Po, G. Bianchi, A. Cominetti, C. Carbonera, N. Camaioni, F. Tinti, J. Kong, *PNAS*, 2019, **116**, 22037-22043.

19. E. M. Speller, *Mater. Sci. Tech.* 2019, **33**, 924-933.

20. G. Liu, J. Jia, K. Zhang, X. E. Jia, Q. Yin, W. Zhong, L. Li, F. Huang, Y. Cao, *Adv. Energy Mater.* 2019, *9*, 1803657.

21. D. C. Olson, S. E. Shaheen, M. S. White, W. J. Mitchell, M. F. A. M. van Hest, R. T. Collins and D. S. Ginley, *Adv. Funct. Mater.*, 2007, **17**, 264–269.

22. D. Qian, Z. Zheng, H. Yao, W. Tress, T. R. Hopper, S. Chen, S. Li, J. Liu, S. Chen, J. Zhang, X.-K. Liu, B. Gao, L. Ouyang, Y. Jin, G. Pozina, I. A. Buyanova, W. M. Chen, O.

Inganäs, V. Coropceanu, J.-L. Bredas, H. Yan, J. Hou, F. Zhang, A. A. Bakulin and F. Gao, *Nat. Mater.*, 2018, **17**, 703–709.

23. A. Wadsworth, M. Moser, A. Marks, M. S. Little, N. Gasparini, C. J. Brabec, D. Baran and I. McCulloch, *Chem. Soc. Rev.*, 2018, **48**, 1596–1625.

24. W. Wang, B. Chen, X. Jiao, J. Guo, R. Sun, J. Guo, J. Min, *Org. Electron.* 2019, **70**, 78-85.

25. F. J. Lim, A. Krishnamoorthy, G. W. Ho, *Sol. Energy Mater. Sol. Cells*, 2016, **150**, 19-31.

26. S. Rafique, S. M. Abdullah, K. Sulaiman, M. Iwamoto, *Renewable and Sustainable Energy Reviews*, 2018, **84**, 43-53.

27. Z. Zhang, J. Miao, Z. Ding, B. Kan, B. Lin, X. Wan, W. Ma, Y. Chen, X. Long, C. Dou, J. Zhang, *Nat. Commun.* 2019, **10**, 1-8.

28. Z. Yang, T. Zhang, J. Li, W. Xue, C. Han, Y. Cheng, L. Qian, W. Cao, Y. Yang, S. Chen, *Sci. Rep.* 2017, **7**, 1-9.

29. R. Wang, M. Mujahid, Y. Duan, Z. K. Wang, J. Xue, Y. Yang, *Adv. Funct. Mater.* 2019, **29**, 1808843.

30. J. Wei, C. Zhang, G. Ji, Y. Han, L. Ismail, H. Li, Q. Luo, J. Yang, C. Q. Ma,. *Sol. Energy*, 2019, **193**, 102-110.

31. S. Rafique, N. A. Roslan, S. M. Abdullah, L. Li, A. Supangat, A. Jilani, M. Iwamoto, *Org. Electron.* 2016, **66**, 32-42.

32. M. Hilal, J. I. Han, *Sol. Energy*, 2018, **167**, 24-34.

33. M. M. Tavakoli, M. H. Gharahcheshmeh, N. Moody, M. G. Bawendi, K. K. Gleason, J. Kong, *Adv. Mater. Interfaces*, 2020, 2000498.

34. M. M. Stylianakis, D. Konios, C. Petridis, G. Kakavelakis, E. Stratakis, E. Kymakis, *2D Mater.* 2017, **4**, 042005.

35. E. Singh, K. S. Kim, G. Y. Yeom, H. S. Nalwa, *ACS Appl. Mater. Interfaces*, 2017, **9**, 3223-3245.

36. M. M. Tavakoli, G. Azzellino, M. Hempel, A. Y. Lu, F. J. Martin-Martinez, J. Zhao, J. Yeo, T. Palacios, M. J. Buehler, J. Kong, *Adv. Funct. Mater.* 2020, 2001924.

37. G. Kakavelakis, A. E. Del Rio Castillo, A. Ansaldo, P. Tzourmpakis, R. Brescia, M. Prato, E. Stratakis, E. Kymakis and F. Bonaccorso, *ACS Nano*, 2017, **11**, 3517–3531.

38. M. M. Tavakoli, M. Nasilowski, J. Zhao, M. G. Bawendi, J. Kong, *Small Methods*, 2019, **3**, 1900449.

39. K. Petridis, G. Kakavelakis, M. M. Stylianakis, E. Kymakis, *Chemistry–An Asian Journal*, 2018, **13**, 240-249.

40. M. M. Tavakoli, R. Tavakoli, P. Yadav, J. Kong, *J. Mater. Chem. A*, 2019, **7**, 679-686.

41. K. Noori, D. Konios, M. M. Stylianakis, E. Kymakis, F. Giustino, *2D Materials*, 2016, **3**, 015003.

42. E. Singh, K. S. Kim, G. Y. Yeom, H. S. Nalwa, *ACS applied materials & interfaces*, 2017, **9**, 3223-3245.

43. N. Izyumskaya, D. O. Demchenko, S. Das, U. Özgür, V. Avrutin, H. Morkoç, *Adv. Electron. Mater.* 2017, **3**, 1600485.

44. L. Liu, Y. P. Feng, Z. X. Shen, *Phys. Rev. B*, 2003, **68**, 104102.

45. J. Duan, X. Wang, X. Lai, G. Li, K. Watanabe, T. Taniguchi, M. Zebarjadi, E. Y. Andrei, *PNAS*, 2016, **113**, 14272-14276.

46. M. M. Tavakoli, H. T. Dastjerdi, J. Zhao, K. E. Shulenberger, C. Carbonera, R. Po, A. Cominetti, G. Bianchi, N. D. Klein, M. G. Bawendi, S. Gradecak, J. Kong, *Small* 2019, **15**, 1900508.

47. M. D. Irwin, D. B. Buchholz, A. W. Hains, R. P. Chang, T. J. Marks, *PNAS*, 2008, **105**, 2783-2787.

48. M. M. Tavakoli, H. T. Dastjerdi, D. Prochowicz, P. Yadav, R. Tavakoli, M. Saliba, Z. Fan, *J. Mater. Chem. A*, 2019, **7**, 14753-14760.

49. M. O. Reese, S. A. Gevorgyan, M. Jørgensen, E. Bundgaard, S. R. Kurtz, D. S. Ginley, D. C. Olson, M. T. Lloyd, P. Morvillo, E. A. Katz, A. Elschner, *Sol. Energy Mater. Sol. Cells*, 2011, **95**, 1253-1267.

In this study, we fabricate efficient inverted organic photovoltaics using h-BN as an electron blocking layer and improve the device stability as compared to the reference devices.